Seismicity modulation due to hydrological loading in a stable continental region: a case study from the Jektvik swarm sequence in Northern Norway

Hasbi Ash Shiddiqi [1], Lars Ottemöller,[1] Stéphane Rondenay,[1] Susana Custódio,[2] Vineet K. Gahalaut [3], Rajeev K. Yadav,[3] Felix Halpaap[1] and Kalpna Gahalaut[3]

[1]*Department of Earth Science, University of Bergen, 5007 Bergen, Norway. E-mail: hasbi.shiddiqi@uib.no; h.a.shiddiqi@gmail.com*
[2]*Instituto Dom Luiz, Faculdade de Ciências, Universidade de Lisboa, 1749-016 Lisboa, Portugal*
[3]*CSIR-National Geophysical Research Institute, 500007 Hyderabad, India*

SUMMARY

Seismic swarms have been observed for more than 40 yr along the coast of Nordland, Northern Norway. However, the detailed spatio-temporal evolution and mechanisms of these swarms have not yet been resolved due to the historically sparse seismic station coverage. An increased number of seismic stations now allows us to study a nearly decade-long sequence of swarms in the Jektvik area during the 2013–2021 time window. Our analysis resolves four major groups of seismic events, each consisting of several spatial clusters, that have distinct spatial and temporal behaviours. Computed focal mechanism solutions are predominantly normal with NNE–SSW strike direction reflecting a near-vertical maximum principal stress and a NW–SE near-horizontal minimum principal stress, which are controlled by local NW–SE extension. We attribute the swarms to fluid-saturated fracture zones that are reactivated due to this local extension. Over the time period, the activity tends to increase between February and May, which coincides with the late winter and beginning of spring time in Norway. We hypothesize that the seismicity is modulated seasonally by hydrological loading from snow accumulation. This transient hydrological load results in elastic deformation that is observed at local Global Navigation Satellite System stations. The loading is shown to promote failure in a critically stressed normal faulting system. Once a segment is activated, it can then also trigger neighboring segments via stress transfer. Our new results point to a close link between lithosphere and hydrosphere contributing to the occurrence of seismic swarm activity in northern Norway.

Key words: Arctic region; Europe; Seismicity and tectonics; Intra-plate processes; Continental tectonics: extensional.

1 INTRODUCTION

The coastal region of Nordland, northern Norway, experiences considerable earthquake swarm activity, which does not show a clear mainshock-aftershock relation. The swarms are situated within one of the most seismically active regions in mainland Norway, where more than 200 earthquakes above M_L 0.5 are recorded annually and which also hosted one of the largest documented earthquakes in Fennoscandia: the 1819 M 5.9 Lurøy earthquake (Muir-Wood 1989; Bungum & Olesen 2005; Mäntyniemi *et al.* 2020; Fig. 1a). Many seismic activities, including swarms, have been reported here over the past few decades, including those of Meløy in 1978–1979 (Bungum *et al.* 1979, 1982), Steigen in 1992 (Atakan *et al.* 1994), Rana in 1998–1999 and 2005 (Hicks *et al.* 2000; Gibbons *et al.*

2007) and Jektvik in 2015-2016 (Michálek *et al.* 2018). Although some hypotheses to explain the regional seismicity in Nordland have been proposed, a detailed characterization of these swarms has not been possible until now due to the sparsity of seismic stations. Addressing this shortcoming is important as swarms have the potential to help us better understand deformation in the region and the physical properties of the crust. These results can then be utilized to improve seismic hazard assessment in an intraplate region with historical large earthquakes and smaller present-day seismicity, including seismic swarms (e.g. Liu & Stein 2016; Stein *et al.* 2017; Matos *et al.* 2018).

The Nordland region has been shaped by a series of major geological episodes. The collision between Baltica and Laurentia resulted in the Caledonian orogeny with high mountains between the late
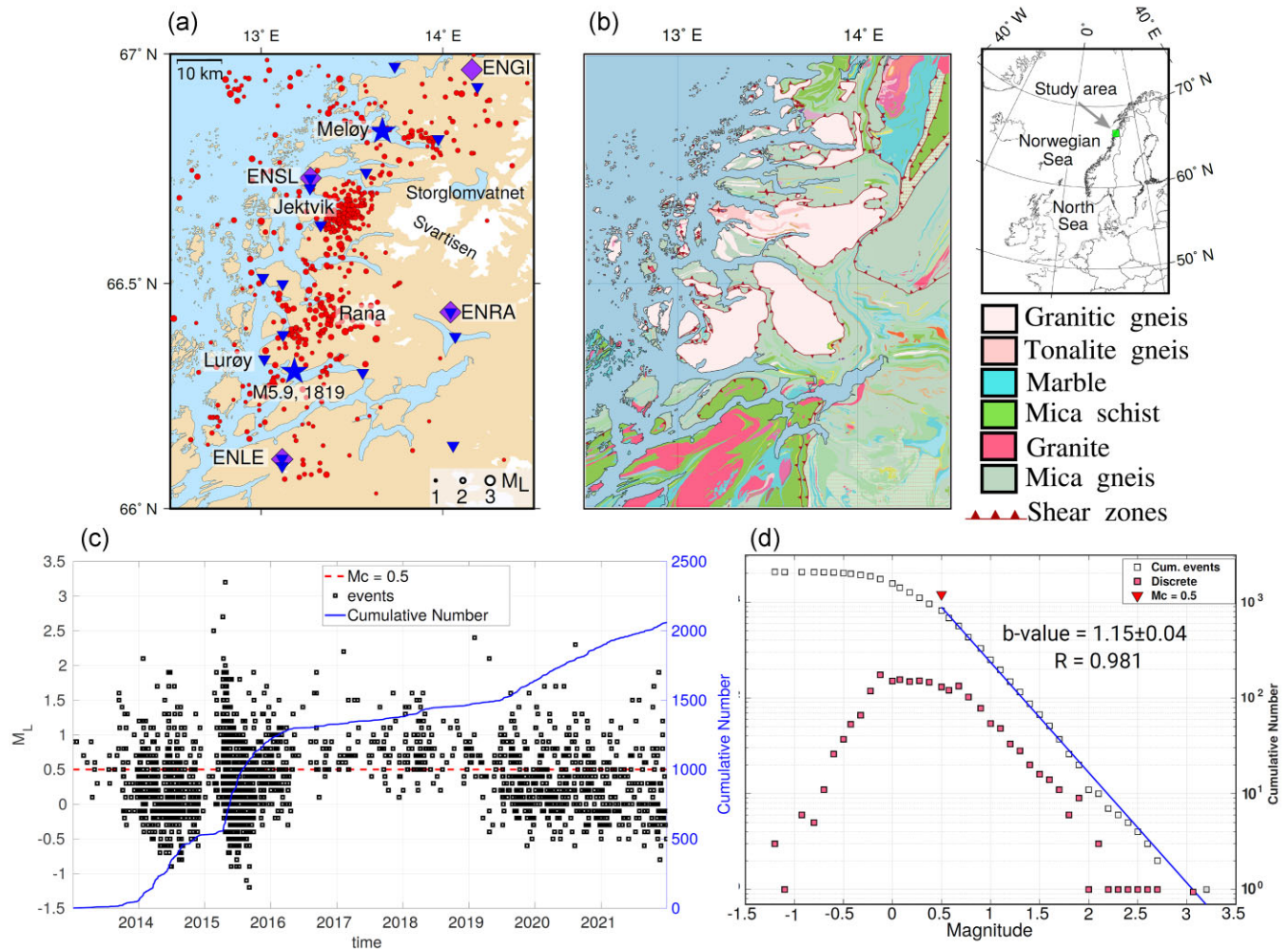
Figure 1. (a) Seismicity maps ($M_L \geq 1.0$) in Jektvik and nearby regions. Epicenters are shown as red circles. Notable previous seismic events are marked as blue stars: the estimated location of the M 5.9 1819 Lurøy earthquake and the center of the 1978–1979 Meløy swarms. Seismic and GNSS stations (ENSL, ENGI, ENRA and ENLE) used in this study are depicted as blue inverted triangles and purple diamonds, respectively. Storglomvt: Storglomvatnet water reservoir. (b) Bedrock geology map for the area from the National Bedrock Database from Geological Survey of Norway (2011). Inset map shows the location of the study area in a larger geographical context. (c) Temporal variation of earthquakes with M_L and cumulative number of earthquakes. The magnitude of completeness (Mc = 0.5) is shown as dashed red line. (d) Frequency magnitude distribution of the catalogue. The b-value for the whole data set is 1.15.

Cambrian and early Devonian (e.g. Tsikalas *et al.* 2001; Corfu *et al.* 2014). It was followed by orogenic collapse in the Devonian and then rifting during the opening of the North Atlantic Ocean. Nordland is part of the Caledonian domain, which is dominated by nappe complexes as a result of the collision (Corfu *et al.* 2014). The area is mostly covered by the Upper and Uppermost Allochthons, which were thrust onto the Precambrian basement (Roberts 1988; Corfu *et al.* 2014). Following the collapse of the Caledonides, extensional shear zones and detachment faults were formed (Fossen 2010). Part of the Jektvik area, which is the focus in this study, consists of Precambrian granitoids dominated by granitic and tonalite gneiss (Fig. 1b). The dominant strikes of extensional faults and shear zones in the area are NNE–SSW and WNW–ESE (Fig. 1b). This is supported by detailed mapping of the Jektvik region, which identified a small shear zone and a set of fractures with dominant NNE–SSW and WNW–ESE directions (Rostad 1990).

Earthquake fault plane solutions and geodetic observations indicate a rather complex stress regime in Nordland and the adjacent offshore areas. While the mechanisms of earthquake located along the shelf edge are mainly characterized by thrust faulting, those

of earthquakes located along the coast are dominated by normal faulting (Janutyte *et al.* 2017; Michálek *et al.* 2018; Shiddiqi *et al.* 2022). The normal faulting events along the coast reflect a deviation from the compressive regional stress, which possibly arises due the additional interference from glacial isostatic adjustment (GIA) and sediment redistribution (e.g. Bungum *et al.* 2010; Gradmann *et al.* 2018). Nordland is rising due to GIA, with an average uplift rate of around 4 mm yr^{-1} in the coastal area (Kierulf *et al.* 2014). Furthermore, the differences between Global Navigation Satellite System (GNSS) observations and GIA models in Nordland are larger than in other parts of Scandinavia, which may indicate strong subsurface lateral heterogeneity or neotectonic processes (Kierulf *et al.* 2014; Kierulf 2017).

Intraplate seismic swarms in various stable continental regions (SCR) worldwide can offer clues as to what causes swarms in Nordland. Swarms are often attributed to the reactivation of pre-existing faults under regional and local stress conditions (e.g. Talwani 2017). Fluids can play an important role in facilitating seismic swarms by reducing the normal stresses via pore-pressure increase. In addition, hydrological load changes from water bodies, soil moisture

and snow cause elastic deformation, which often is observable in GNSS data (e.g. Drouin *et al.* 2016; Springer *et al.* 2019). The load change can be significant enough to modulate stresses, pore-pressure and eventually seismic rupture, as suggested by Hainzl *et al.* (2006), Craig *et al.* (2017) and Gahalaut *et al.* (2022). Possible links between hydrological processes and swarms have been inferred in various intraplate regions, notably Mt. Hochstaufen in Germany (Hainzl *et al.* 2006), New Madrid in the USA (Bisrat *et al.* 2012) and Palghar in Western India (Sharma *et al.* 2020; Gahalaut *et al.* 2022). In case of Nordland, Maystrenko *et al.* (2020) suggested a link between rainfall and seismicity. In order to investigate the possible role of hydrological processes in Nordland, we first need to characterize precisely the spatio-temporal evolution of seismicity - something that has not been possible until now.

In this study, we take advantage of improved station coverage to investigate the spatio-temporal distribution of the sequence of swarms in Jektvik, which has been active for more than 9 yr. Our objective is to develop a high resolution earthquake catalogue, supplemented with computations of focal mechanisms. We improve the existing earthquake catalogue by adding previously undetected seismic events using a deep-learning based algorithm. Then we relocate the earthquakes and identify spatial clusters using differential times and waveform similarity. Using the high-quality seismicity and computed focal mechanisms solutions, we image the fault systems corresponding to the regions where the swarms occurred. We finally use these results to investigate the possible processes that can trigger the swarms and the mechanisms that cause seismicity to migrate within and between fault segments.

2 IMPROVING THE EARTHQUAKE CATALOGUE

To date, swarm activity in Nordland has been characterized mainly using relatively sparse permanent stations, which usually results in catalogues with magnitude of completeness ≥ 1.0. This is clearly insufficient to investigate the processes responsible for swarm activity. To address this shortcoming, we developed a high-quality earthquake catalogue for Nordland by combining data from permanent stations with those from temporary stations deployed in the region over the past decade. Using this new expanded data set, we first performed automatic seismic event detection and phase picking to process events that have not been reported in the Norwegian National Seismic Network (NNSN) catalogue (Ottemöller *et al.* 2018). Then we performed manual phase checking, hypocenter location and local magnitude determination using SEISAN software package (Havskov & Ottemoller 1999; Havskov *et al.* 2020).

To establish a comprehensive data set, we collected and integrated relevant catalogues and waveform data from temporary and permanent seismic stations. As a starting database, we used the NNSN earthquake catalogue in the 2013–2021 time window (with a cutoff year set at 2013 because station coverage was too sparse prior to that). The number of stations in the region has grown significantly since 2013 owing to the deployment of two temporary networks: Neonor2, 2013–2016 (Michálek *et al.* 2018) and Scanlips3D, 2013–2014 (England *et al.* 2016). Since 2018, the NNSN has added six permanent stations in Nordland within 150 km of Jektvik. These changes have resulted in a variable station coverage over time that can be appraised by compiling the monthly number of stations operating within 150 km from the study area over the 2013–2021 period (see Fig. S1). The number of stations reached a maximum of 36 in 2014 and a minimum of 4 between 2016 June and 2018 October,

which resulted in a slightly decreased detection capability during this latter time window. It will be important to be aware of these fluctuations when we assess the magnitude of completeness of the whole catalogue.

The integration of the various data sets allowed us to expand the existing catalogue (a product of routine processing by the NNSN) by adding smaller earthquakes. This was done by utilizing the Eq-transformer Python package (Mousavi *et al.* 2020), a powerful deep-learning based tool employed for seismic event detection and phase picking. The picker is trained using the STanford EArthquake Data set (STEAD; Mousavi *et al.* 2019), consisting of a global earthquake database that includes data from a few Norwegian earthquakes. Despite the fact that the picker was trained using mostly data from other regions, previous studies have shown that it can perform well under such conditions (e.g. Mousavi *et al.* 2020; Jiang *et al.* 2022; Münchmeyer *et al.* 2022). An example of event detection and phase picking for events with M_L 0.4 and M_L −0.8, recorded by the station closest to the Jektvik swarm (N2VG), is shown in Fig. S2. For each event detected and processed by Eqtransformer, we used SEISAN to perform a manual check of recordings from all available stations and to pick phase arrivals that may have been missed by the routine automated workflow. After verification, the newly detected events were merged with the NNSN catalogue. We used events that were detected both by NNSN and Eqtransformer to evaluate the accuracy of the automatic picking results and estimate the picking errors for the whole catalogue. Based on this comparison, we found that the mean difference between NNSN and Eqtransformer phase picks is 0.12 s for P-waves and 0.14 s for S-waves (Fig. S3) and conclude that manual and Eqtransformer processing are compatible. This is essential for further processing and interpretation of the combined catalogue.

For the set of detected events we initially determined hypocenter locations by travel-time inversion using the Hypocenter program (Lienert & Havskov 1995). The program requires a velocity model to compute travel-times; we used the minimum 1D velocity model developed for the Nordland region by Shiddiqi *et al.* (2022). We estimated the location errors using a bootstrap resampling analysis similar to that of Shiddiqi *et al.* (2019), in which the inversion procedure was repeated 100 times by adding random Gaussian noise with a standard error of 0.2 s to the arrival times and recomputing the hypocenter locations. Error estimates were then computed by taking the standard deviation of the 100 realizations in the horizontal (σ_H) and vertical directions (σ_V). In order to get reliable hypocenters without discarding large number of earthquakes, the events retained for further processing and interpretation are chosen based on a set of somewhat relaxed selection criteria: (1) a minimum of five picks with at least two S-picks, (2) azimuthal gap $\leq 225°$ and (3) both σ_H and $\sigma_V \leq 5.0$ km. A total of 2063 events fit these criteria, including 1095 newly detected earthquakes. The histograms of σ_H and σ_V are shown in Fig. 2 and the mean of σ_H and σ_V are 1.14 and 1.57 km, respectively.

We measured earthquake size for all detected earthquakes by computing local magnitudes, M_L, using the scale for Norway (Al-saker *et al.* 1991). This is achieved by measuring the maximum amplitudes of Sg waves on simulated Wood-Anderson traces of the vertical channels that are filtered between 2.0 and 18.0 Hz. We chose this frequency band because it yields considerably higher signal-to-noise ratio for small earthquakes compared to the standard frequency band of 1.25–18 Hz applied by the NNSN; see Havskov & Ottemöller (2010). The amplitude measurements were performed automatically using the Automag program in SEISAN. To mitigate M_L overestimation at short-distance stations, we added a correction
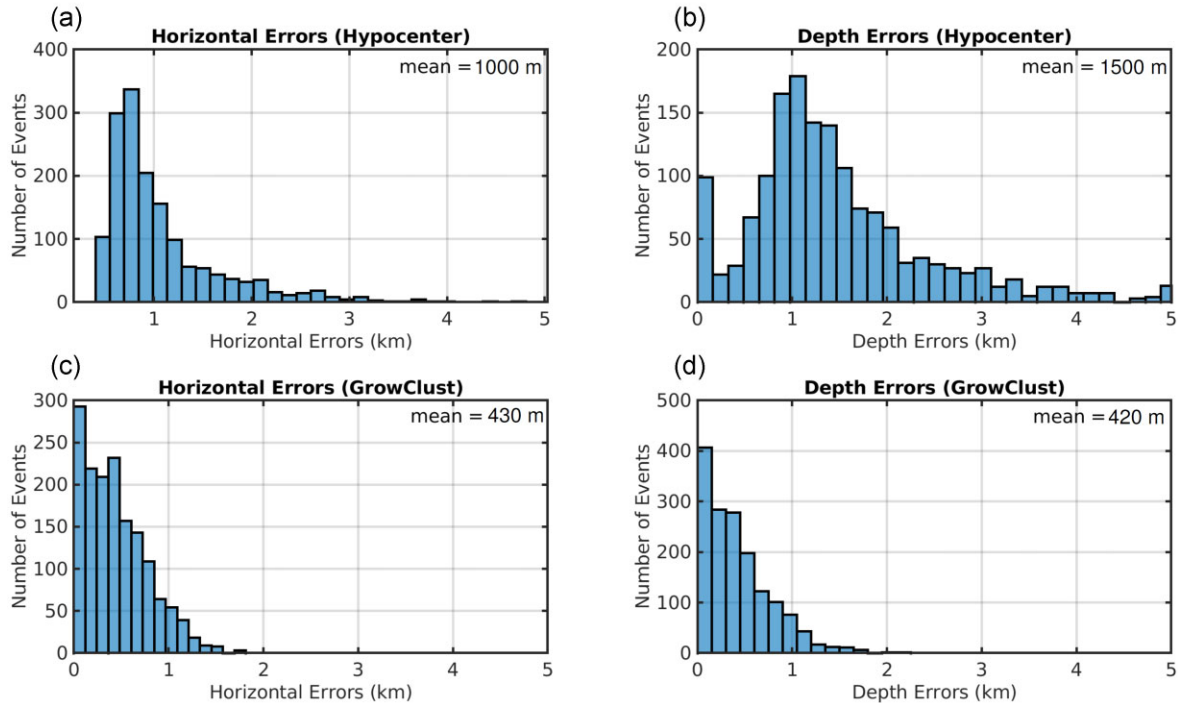
Figure 2. Comparison of initial and relative location errors estimated using a bootstrap resampling method. Histograms of σ_H and σ_V of initial locations shown in (a) and (b). Only earthquakes relocated by GrowClust program are presented here. Histograms of relative location σ_H and σ_V determined using GrowClust program are shown in (c) and (d).

term for Northern Norway: $-0.74e^{0.09r}$, where r is distance in km (Luckett *et al.* 2018). With this correction, the M_L scale for Northern Norway becomes

$$M_L = log(amp) + 0.91log(r) + 0.00087r - 0.74e^{0.09r} - 1.67 \quad (11)$$

where *amp* is the amplitude on the Wood-Anderson seismogram in nanometers. The magnitude-frequency distribution of the improved catalogue gives an overall b-value of 1.15 and a magnitude of completeness (M_c) of M_L 0.5 (Fig. 1d).

We computed focal mechanisms for events after May 2016 to complement previous studies that had computed fault plane solutions for earthquakes between 2013 August and 2016 May in the Jektvik area (Shiddiqi *et al.* 2022). We used first motion polarities picked on unfiltered vertical traces, as well as amplitudes of direct Pg and Sg waves from distances ≤100 km measured on the vertical and transverse traces, respectively. The Pg and Sg amplitudes were corrected for crustal attenuation and free surface. To correct for attenuation, we adopted the Q value for mainland Norway $Q_{Lg} = 529 f^{0.42}$ (Demuth *et al.* 2019) and assumed that Q_P and Q_S have the same value. Following Shiddiqi *et al.* (2022), we computed the take off angles using a 3D V_P model for Nordland, which has been shown to improve the solutions. The focal mechanisms were estimated using the Focmec program (Snoke 2003). Due to the relatively small number of stations, we set more relaxed acceptable solution criteria than Michálek *et al.* (2018); Shiddiqi *et al.* (2022). We did not allow for any polarity error and the acceptable amplitude ratios were required to have a logarithmic misfit less than 0.2; see the Focmec manual (Snoke 2017). Of the computed mechanisms, we retained those that satisfy the following criteria: (1) the input data include at least five polarities covering both compression and dilatation quadrants of the focal sphere, (2) more than half of the

observations must yield acceptable amplitude ratios and (3) all solutions obtained for one event have to be similar: P- and T-axes concentrate within $\sim \frac{1}{10}$ areas on the focal sphere.

3 HYPOCENTER RELOCATION AND CLUSTERING

To improve the locations of events and assess objectively their degree of clustering, we employed the GrowClust relocation program that combines earthquake relocation and hierarchical clustering (Trugman & Shearer 2017). We refer to a group of earthquakes as cluster due to their spatial proximity as indicated by high waveform cross-correlation coefficients (CC). Identification of clusters, in our case spatial clusters, helps to identify the fault segments and to characterize the spatio-temporal behaviour of the seismicity. As input data, Growclust uses travel-time differences and CC for event pairs recorded on single stations. We used the Obspy package (Beyreuther *et al.* 2010; Krischer *et al.* 2015; Megies *et al.* 2019) to carry out key pre-processing operations on the input waveforms, including instrument response removal and band-pass filtering between 3.0 to 9.0 Hz and then the EQcorrscan package (Chamberlain *et al.* 2017) to compute the travel-time differences and waveform correlations. We computed correlations of event pairs with maximum separation of 10 km.

The Growclust algorithm employs a grid-search approach to minimize the L1 norm, which is least sensitive to outliers of travel-time residuals within a cluster. GrowClust uses a 1D velocity model to compute the synthetic travel-times for direct arrivals (i.e. Pg and Sg) and does not take into account Moho refracted arrivals (i.e. Pn and Sn). Therefore, we selected observations from stations closer than the cross-over distance of 150 km in our case. Event clusters were identified using a hierarchical clustering algorithm in GrowClust,

where events are paired based on a number of criteria: minimum CC cutoff (rmin), maximum root-mean-square of travel-time residuals (rmsmax) and distance. We tested a number of rmin values to find the preferred value. The rmsmax was set to a value of 0.2 s, which was found to be suitable in previous studies (Trugman & Shearer 2017; Ross *et al.* 2020). Relaxing the rmsmax value can increase the number of relocated events, but at the same time reduce the relative location quality. We allowed events to join a cluster if they are separated by no more than 8 km distance in the initial catalogue and 4 km distance in the relocated catalogue. The relocation uncertainties (σ_H and σ_V) were estimated using bootstrap resampling method, which is integrated within the GrowClust algorithm. Furthermore, we evaluated clustering robustness by inspecting earthquake distribution and the hierarchical clustering trees (dendrogram), which show the links between events by means of CC and event clustering.

4 RESULTS

The analysis described in the previous sections yields an improved earthquake catalogue that contains differential times, cross correlations, amplitudes and polarities. This provides us with more accurate relative locations, cluster identification, fault plane solutions and magnitude estimates. In total we relocated 1590 events. On average, each event location was determined by more than 200 differential times. The quality of the relative locations is best expressed via the reduction in location error compared to the initial hypocenters (Fig. 2). The average σ_H and σ_V of the relocated earthquakes are 430 and 420 m, respectively, in comparison to 1000 and 1500 m for their initial absolute locations. To ensure the reliability of our analysis, we only use events below the 95th percentile of the location errors, that is, less than 1000 m (for the complete catalogue including unrelocated events, see the data availability section).

Our relocation results allow us to resolve the details of the seismicity. We obtained 11 clusters that contain ≥25 events. To simplify the description of the spatio-temporal evolution of the seismicity, we combined the clusters into four main groups based on their location, that is, A – center of the activity, B – southwestern part, C – eastern part and D – northeastern part (Fig. 3). We evaluated the event clustering using CC matrices and the links between events using dendrogram. As an example, Fig. 4 shows that group B consists of three individual clusters (B1, B2 and B3), which is consistent with the GrowClust clustering result.

Swarm activity in Jektvik started in 2013 with Group A, which has remained active throughout the period of investigation. Group A is seen as the center of the swarm and eventually developed into four major clusters. Sharp increases in activity for this group were seen in early 2014 and early 2015. Most of the seismicity in this group occurred beneath or nearby Tjongsfjorden. From 2013 to early 2015, areas outside Group A were relatively quiet, but from 2015 April, a new set of earthquakes (Group B) started to appear southwest of Group A. Cluster B1, where the largest event of the whole sequence (M_L 3.2) occurred, was confined in space and time, with most of the seismicity occurring over a two month period. Cluster B2 was located further to the southwest by more than 7 km from the center of Group A and became active a few days after B1. This cluster was also confined in space, but not so much in time, lasting for more than 1 yr. Cluster B3, with an epicentral trend parallel to cluster B1, became active as well during this period, eventually ending in 2016. In 2019, a new patch of seismicity appeared to the southeast of the swarm center forming Group C, which remained active for 3.5 yr. Other areas were not very active between 2016 and 2018, although

smaller earthquakes would have been missed during this time due to the reduced number of stations. Since 2019, a significant change in the spatial distribution of earthquakes has occurred with the appearance of group D, which is located near the northeastern edge of group A from where it has expanded progressively in a north-northeast direction. By the end of 2021, the Group D hypocenters were located 6.8 km away from the center of Group A. The total extent of the swarm activity is ca. 14 km in SW-NE and ca. 6 km in NW–SE direction, giving a total area of ca. 84 km^2.

We attempted to compute the focal mechanisms of 20 events that occurred after mid-2016 and found three solutions that were deemed acceptable. After mid-2016, stations are fewer, which makes obtaining good solutions challenging. The three solutions from this study, together with those by Michálek *et al.* (2018) and Shiddiqi *et al.* (2022) are shown in Fig. 3 and Table 1. These solutions show normal and oblique-normal faulting with strike along NE–SW direction on two possible planes: shallow dipping (20°–40°) and steeply dipping (50°–70°) planes. To constrain the focal mechanisms, we estimated the fault segment geometries (strike and dip) using a principal component analysis on spatial matrices of the identified clusters (Michelini & Bolt 1986; Mesimeri *et al.* 2022). Similar to the focal mechanisms, the principal component analysis for clusters A1, B1, B2 and B3 results in a NE–SW trend with steeply dipping planes (60°–80°; Fig. 5). Hypocenters in group D (clusters D1 and D2) show a nearly NS strike and steeper dipping plane (≥ 80°) than other clusters. Based on these observations, we prefer the steeply dipping fault planes. The stress orientation inferred from the NE–SW striking parallel normal faults indicate near vertical maximum compression (σ_1) and near horizontal minimum compression (σ_3) in the WNW direction.

To gain better insight into the characteristics of the seismicity, we analysed the temporal evolution of the cumulative number of events ($M_L \geq Mc$), the cumulative seismic moment (assuming $M_L = M_w$) and the spatio-temporal distribution of along-strike seismicity (Fig. 6). The 15 largest events are also shown in Fig. 6. The occurrence of the largest events, combined with a sequence of sharp increases in cumulative event number and seismic moment, indicate that activity prior to mid-2016 was higher than afterwards. In several clusters, there is a delay between the sharp increases in seismic moment and cumulative event number. The sharp increase in cumulative seismic moment tends to generally occur earlier, which indicates that the larger magnitude events occur relatively early within a swarm and are then followed by many smaller earthquakes. We identified the initiation of seismic activity by observing the change of seismicity rate following Schoenball & Ellsworth (2017). We identified 12 increasing seismic activity, where nine of them initiated between February and May, coinciding with the northern hemisphere late winter and spring time (Fig. 6 and Figs S9, S10 and S11 in the supporting information), hinting at a possible seasonality in the seismic activity of the region.

In order to characterize physical properties, we compiled statistics for each cluster (see Table 2): duration, maximum M_L, total seismic moment and the M_w equivalent of all events. Table 2 shows that the activity duration for each cluster varies indicating distinct temporal behaviour. We look at the size of the complete seismic activity between 2013 and 2021. The total seismic moment for the whole catalogue is 1.54 E+14 Nm, which is equivalent to M_w 3.4. We can alternatively estimate the seismic moment from the extent of the faults. The seismicity is distributed onto a number of fault segments, which in total encompass an 11 km NNE–SSW elongated line. If we look in detail at individual segments, for example group B, clusters B1, B2 and B3 cover areas of approximately 9, 5 and
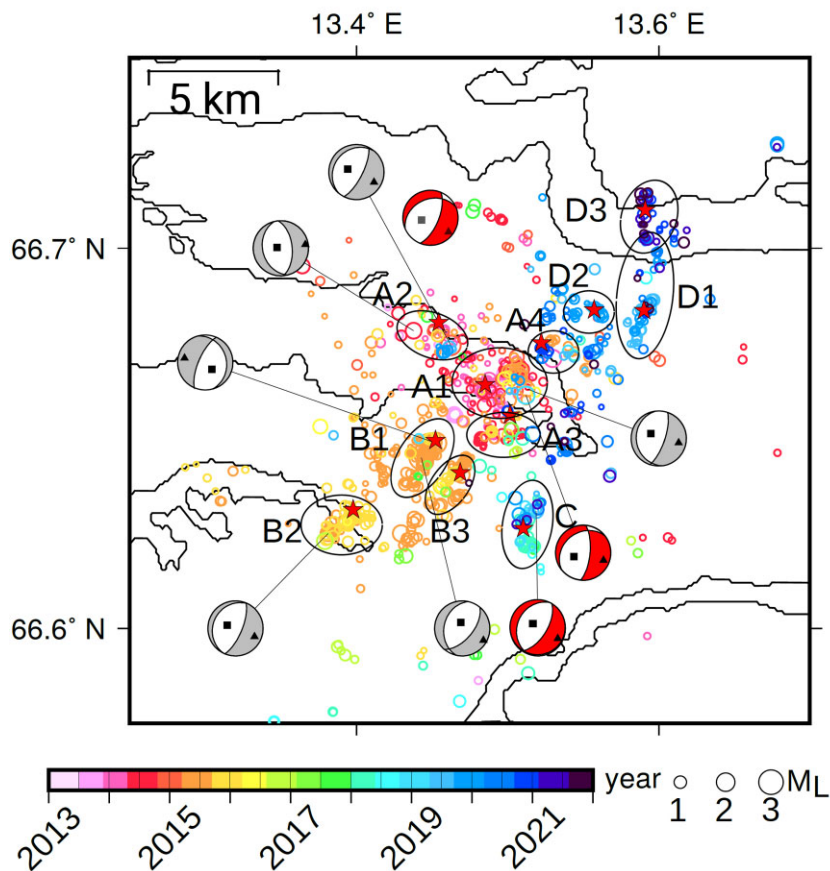
Figure 3. Relocated earthquakes ($M_L \geq 0$) and focal mechanism solutions in Jektvik for the period of 2013–2021. Epicenters are shown as open circle colored with time of occurrence. The major clusters that contain more than 25 events are marked with ellipses. The first event in each cluster is marked as red star. Focal mechanism solutions computed in this study are shown as red fault planes and solutions computed by Shiddiqi *et al.* (2022) are shown gray fault planes. The P- and T-axes of the focal mechanisms are shown as black squares and triangles, respectively.

5 km², respectively. These correspond to M_w 5.1, 4.9 and 4.9 based on the scaling relationship for SCR earthquakes of Leonard (2010). However, the total moment releases for these clusters correspond to M_w of 3.27, 2.15 and 2.41, which means that only small parts of the fault segments failed.

5 DISCUSSION

The spatio-temporal evolution of the Jektvik swarm sequence shows distinct behaviour in terms of activity duration and spatial distribution. In addition it possibly shows physical connection between various clusters. To better understand the characteristics and causes of the swarm, we address the following questions: (1) How does the sequence fit into the regional geological framework and crustal stress? (2) What triggers the seismicity and causes the seasonality? and (3) How do the clusters interact and influence each other?

5.1 Seismicity relation to geology and crustal stress

The seismicity distribution and focal mechanisms highlight NNE–SSW trending fault zones that are dipping either NW or SE. This trend was previously reported in a geotechnical survey undertaken during the planning phase of a road tunnel (Straumdaltunnelen; Rostad 1990), where a NNE–SSW trending shear zone and a number of fractures with NNE–SSW and ESE–WNW strikes were identified

in the area of our Group B. These orientations are also visible in high resolution Digital Terrain Model images (Figs 7 and S4 in the supporting information, from the Norwegian Mapping Authority; Kartverket).

Most of the seismic activity is confined to Precambrian granitic and Tonalite gneiss units (Geological Survey of Norway 2011), which have a high quartz content (e.g. Rutland & Sutherland 1967; Castro 2013). The upper crust, which is shallower than 10 km, of the area has low V_P between 5.2 and 5.7 km s⁻¹, which has been linked to a fractured crust and to the presence of fluids (Shiddiqi *et al.* 2022). Water leakage into a road tunnel is observed several km east of cluster B3 (personal communication, Sølve Utstøl Pettersen, Nordland county), indicating fluid flow within the fracture zones (see Fig. 7 for the tunnel location). A shallow refraction seismic profile located near the tunnel showed that V_P within the fractures dropped 30-40 per cent relative to the surrounding rocks (GEOMAP 1990). Both a fractured crust and a high quartz content indicate weaknesses in the continental crust where strain can localize and have been previously linked to intraplate seismicity (Lowry & Pérez-Gussinyé 2011; Costain 2017). As shown in the result section, the total moment release is relatively small compared to the total area of the activity, suggesting that they represent seismic slip on small fault patches rather than a single large fault.

The underlying driver of the ongoing deformation and resulting earthquakes is given by the present day stress field. As previously shown by Shiddiqi *et al.* (2022), the stress inferred from fault plane
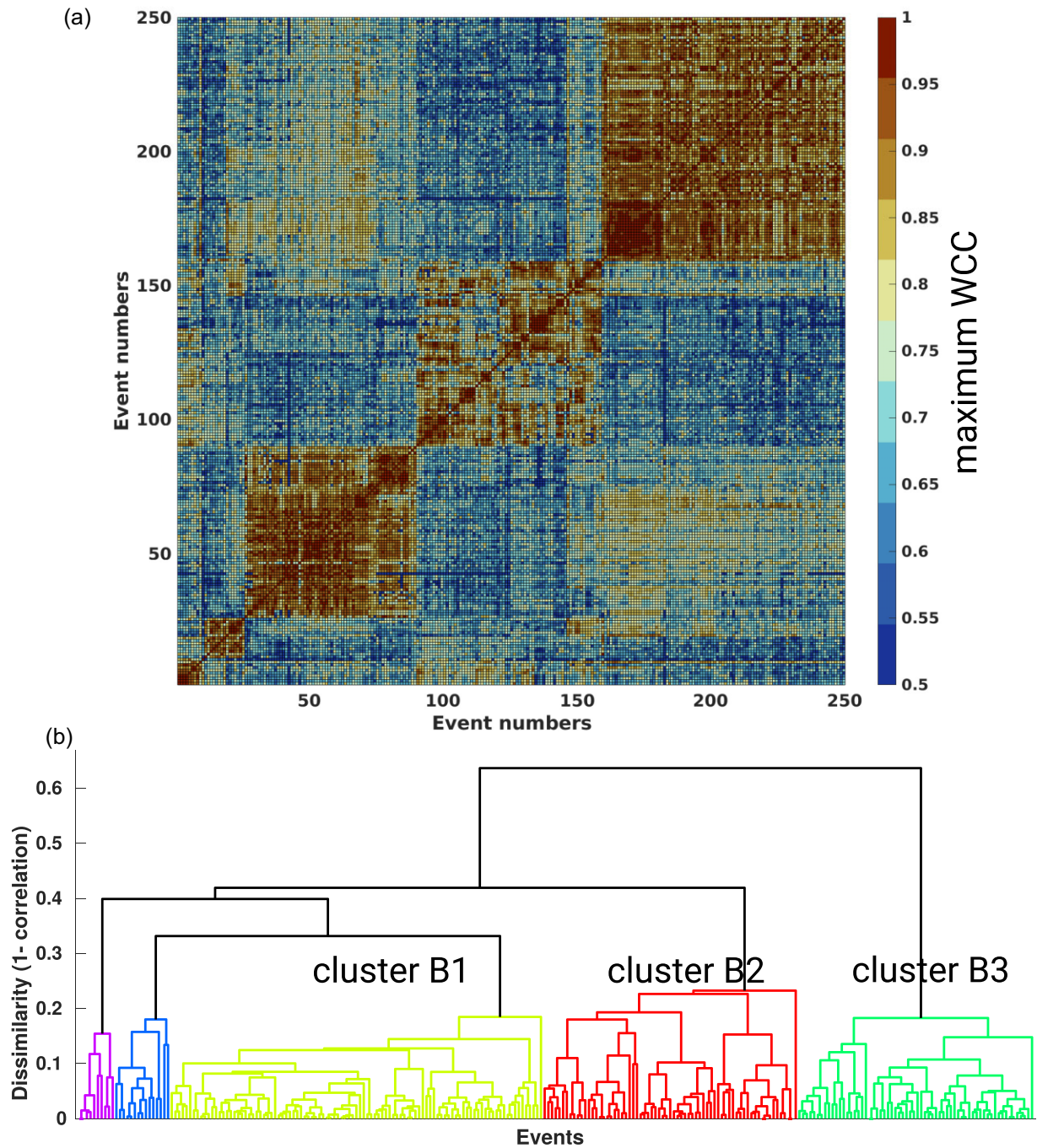
Figure 4. Waveform cross-correlation result and event links for events around group B. (a) sorted CC matrix shows three majors clusters, (b) dendrogram plot, which shows links between events by means of CC, also indicate that there are three majors clusters in Group B.

solutions in the area indicates NW–SE extension, where σ_1 is nearly vertical and σ_3 is subhorizontal in NW direction, which favors the reactivation of NNE–SSW structures. As suggested by previous studies (e.g. Bungum *et al.* 2010; Gradmann *et al.* 2018), this extension likely arises from a combination of glacial isostatic adjustment and sediment redistribution, which overcome the regional compressive stress.

5.2 Triggering factors and cause of modulation

From past studies, we have a reasonable understanding of why there are earthquake swarms in Nordland: failure occurs due to local stresses within fracture zones that are likely fluid saturated, with the fluids potentially bringing the faults closer to rupture. But our analysis of seismicity behaviour shows that this process is not randomly distributed in space and time. Therefore, we explore the existence of

Table 1. Focal mechanisms computed by Shiddiqi *et al.* (2022; marked with ∗) and computed in this study for Jektvik area.

| Date	Time	Latitude	Longitude	Depth (km)	M_L	Strike1/Dip1/Rake1	Strike2/Dip2/Rake2	Solution range
∗2014/06/23	11:04:45	66.678	13.437	8.1	1.9	354.7°/56.1°/−85.2°	166.1°/34.2°/−97.1°	9.8°/4.4°/12.2°
∗2015/02/19	06:00:44	66.689	13.443	4.8	2.5	220.1°/18.4°/−77.3°	26.7°/72.1°/−94.2°	25.4°/4.0°/21.3°
∗2015/04/11	03:13:30	66.665	13.414	3.0	2.6	203.6°/70.6°/−75.1°	344.9°/24.3°/−126.1°	4.1°/3.9°/0.4°
∗2015/04/24	09:40:38	66.639	13.441	3.2	3.2	40.0°/59.0°/−75.0°	192.5°/34.1°/−113.3°	14.1°/4.0°/9.1°
∗2015/05/01	16:03:58	66.663	13.513	6.5	1.7	18.8°/72.2°/−81.6°	173.0°/19.7°/−114.5°	4.4°/7.8°/4.4°
∗2015/07/13	02:58:33	66.640	13.364	9.9	1.9	205.9°/19.0°/−86.9°	22.7°/71.0°/−91.1°	7.7°/3.8°/10.2°
2019/04/23	01:57:33	66.661	13.512	7.8	2.1	231.5°/27.4°/−47.8°	5.4°/69.6°/−109.6°	11.5°/13.6°/16.7°
2019/08/19	05:25:25	66.631	13.519	5.0	1.6	31.1°/62.0°/−87.7°	206.2°/28.1°/−94.3°	6.4°/23.9°/-9.2°
2021/11/15	08/15/46	66.708	13.449	8.2	1.9	247.0°/32.4°/−50.0°	22.2°/65.8°/−112.2°	4.0°/5.8°/7.6°
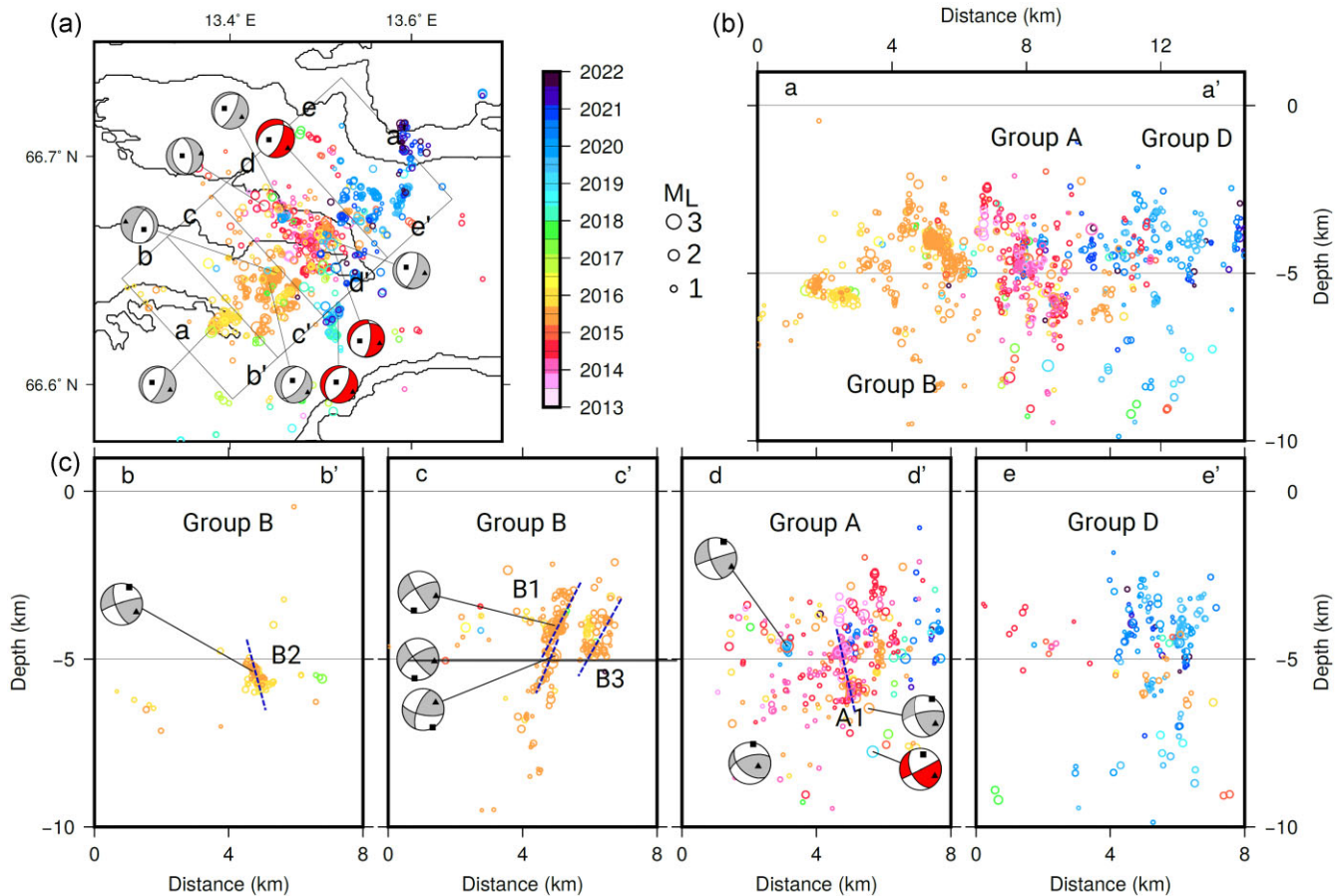
Figure 5. (a) Map view of relocated seismicity, focal mechanisms and position of five profiles: strike parallel (a–a') and perpendicular (b–b' - b–b'). (b)–(c) profiles showing the relocated seismicity and focal mechanisms. The relocated earthquakes ($M_L \geq 0$) are shown as open circles colored based on time of occurrence. Focal mechanisms are plotted in cross-section view, with The P- and T-axes shown as black squares and triangles, respectively. Red and gray fault planes represent solutions computed in this study and by Shiddiqi *et al.* (2022), respectively. Interpreted structures based on seismicity are shown as blue dashed lines.

external processes that may trigger and modulate the seismic activity within and between the different clusters. We expect the modulating process to be of natural origin and, therefore, likely to have a seasonal pattern. When looking at the seasonality of the seismicity, we notice that the initiation of seismic sequences generally occurs between February and May (Fig. 6 and Figs S9, S10 and S11 in the supporting information), corresponding to the end of winter and spring time in Norway. This pattern is also identified from singular spectrum analysis by Shiddiqi *et al.* (2023) that shows a dominant near-annual periodicity for the Jektvik seismicity catalogue. A possible modulating candidate is a change in hydrological load, which has been linked to seismicity in other regions (e.g. Craig *et al.* 2017).

The response of the Earth's surface to changes in hydrological load can be observed with geodetic GNSS data. To investigate the seasonality of the hydrological load, we plotted yearly averaged distributions of normalized earthquake numbers, vertical component GNSS measurements, hydrological loading model (HYDL), snow depth and water reservoir level for the region (Fig. 8). We plotted these data sets in yearly average since the GNSS data around Jektvik are only available from mid-2019. The selected GNSS stations are located within 50 km of the swarm activity (Fig. 1). After removal of the linear trend, the vertical component of GNSS data is rather constant between July and December, but shows a strong decrease, indicating relative subsidence between January and June,
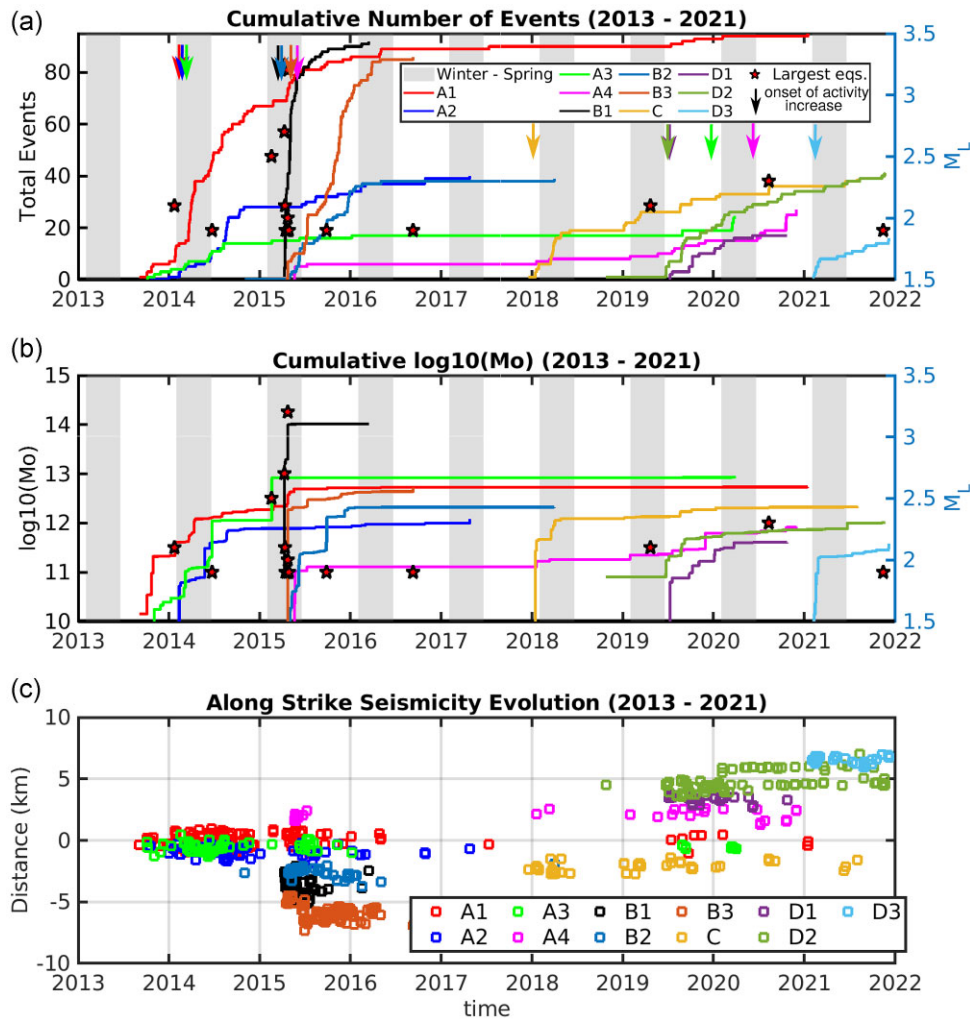
Figure 6. Evolution of earthquake clusters: (a) Cumulative number of events for each cluster, shown as solid lines. Arrows depict the time when the activity began to increase. Red stars depict the 15 largest events. (b) Cumulative log10(Mo) for each cluster. (c) Along strike (NNE–SSW) seismicity migration. The earthquake locations relative to the center of cluster A1 are depicted as open circles colored based on their cluster. Only events with $M_L \geq Mc$ are shown here.

Table 2. Maximum M_L, total seismic moment and the M_w equivalent of all events for each cluster.

Cluster ID	Duration	Largest ML	Total Mo (Nm)	M_w equivalent
A1	88 months	1.9	5.45E+12	2.4
A2	42 months	1.5	1.21E+12	2.0
A3	77 months	2.5	8.64E+12	2.6
A4	66 months	1.6	8.31E+11	1.9
B1	11 months	3.2	1.03E+14	3.3
B2	12 months	1.9	2.11E+12	2.2
B3	16 months	2.0	5.28E+12	2.4
C	42 months	1.6	2.15E+12	2.2
D1	14 months	1.2	4.05E+11	1.7
D2	36 months	1.5	1.02E+12	1.9
D3	9 months	1.2	3.83E+11	1.7

which has a maximum amplitude of −10 mm between February and May. There is a second, but smaller decrease between September and November. The GNSS stations have only been operational for less than 3 yr, but we consider the signals reliable as a similar seasonal variation (although with different amplitudes) is seen on GNSS stations in the broader region of northern Scandinavia (as shown in http://geodesy.unr.edu/NGLStationPages/gpsnetmap/GPSNetMap.html). HYDL is a crustal deformation model derived

from global hydrological constraints (Dill & Dobslaw 2013). For the Jektvik region, it shows the same seasonal pattern as the GNSS data with an estimated maximum ground vertical displacement of −8 mm. The small mismatch between the GNSS data and HYDL estimates is due to the low resolution of the hydrological load model. While the vertical displacement is affected by different processes, for example, tides (Drouin et al. 2016), rainfall (Hsu et al. 2021), our assumption is that the main signal of relative subsidence during
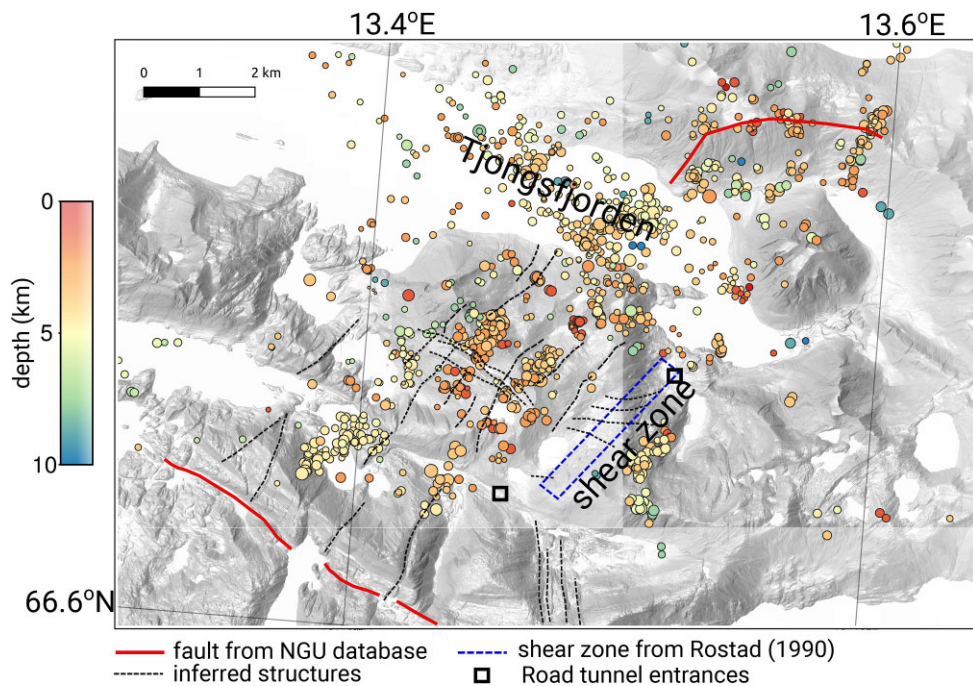
Figure 7. Digital terrain model (DTM) and seismicity for Jektvik area. Interpreted structures are shown as dashed black lines. Approximate location of a shear zone reported by (Rostad 1990) is shown as a blue dashed box. Faults are taken from the National bedrock database provided by the Geological Survey of Norway (NGU; Geological Survey of Norway 2011). The DTM image is provided by the Norwegian Mapping Authority via Geonorge portal (https://www.geonorge.no/).

February–May is caused by the regional snow load, while the secondary signal during September–November could be caused by the maximum filling of water reservoirs in the autumn (as seen for the Storglomvatnet reservoir shown in Fig. 8).

The seasonal peak in seismicity that we identify in Fig. 8(a) coincides with the maximum hydrological load that we ascribe to snow accumulation in the winter. Hydrological loads can be significant enough to cause elastic ground deformation, alter tectonic stress and modulate seismicity, as shown for northeastern Japan by Heki (2003). To test the significance of the static load change from snow accumulation in the area, we followed (Deng *et al.* 2010; Büyükakpınar *et al.* 2021) and modeled 3D Coulomb failure stress changes (ΔCFF). We computed the 3D stress tensor due to surface loading on a half-space elastic media using Boussinesq–Cerruti solutions (see Deng *et al.* 2010). We used a simple snow thickness model that contains two peaks: 2 m in Jektvik and 4 m in the Svartisen glacier area (Fig. 9). Then we computed the changes in shear ($\Delta\tau$) and normal stresses ($\Delta\sigma_n$) for a 45° dip and -90° rake receiver fault due the load. Ignoring the pore-pressure change, ΔCFF is defined as

$$\Delta CFF = \Delta\tau + \mu\Delta\sigma_n \qquad (2)$$

where μ is the friction coefficient that is assumed to be 0.6. From this modeling, we found that snow load increases the ΔCFF on normal faults (Fig. 9) in Jektvik by 1.5–1.8 kPa at depth of up to 8 km. We consider that these changes in hydrological loading are sufficient to trigger seismicity through stress and pore pressure changes (Deng *et al.* 2010; Büyükakpınar *et al.* 2021), even though they are quite small. Previous studies show that small ΔCFF variations (a few kPa) are able to modulate the seismicity (Christiansen *et al.* 2007; Pollitz *et al.* 2013; Craig *et al.* 2017). While the static increase of CFF due to the snow load is instantaneous, the start of seismic activity may be delayed depending on the stress condition. Fig. 6

shows that most of the activity onsets were during the peak of the load suggesting that there was almost no delay or the delay was very short.

The stress modulation affects a larger region, but it can only trigger fault system that are critically stressed and optimally oriented. In the case of Jektvik, such hydrological load is efficient in triggering seismicity owing to the existence of an intricate network of steeply dipping normal faults at shallow depth. With a near vertical σ_1 direction, an increase in hydrological load enhances the tectonic stress most efficiently. It is worth noting that segments were not active at the same time, as shown in the result section, although the same load changes and positive ΔCFF influence them. This temporal variation indicates the variation in the stress condition on the different fault segments. While the hydrological load changes present a tenable trigger mechanism for seismicity in our case, additional work will be needed to model pore-pressure changes and to understand the relative contribution from different processes such as snow cover over the broader region versus higher snow accumulation on glaciers, the filling of reservoirs and changes in the ocean loading. Further investigation to monitor seismic velocity changes using ambient noise is also useful to provide evidence for seasonal pore-pressure changes due to hydrological processes (e.g. Wang *et al.* 2017; Andajani *et al.* 2020).

5.3 Interaction of earthquake clusters

The spatio-temporal evolution of the Jektvik seismicity described in the result section indicates further interaction and triggering within and between clusters, which can be explained by co-seismic ΔCFF. While the hydrological load change appears to be a likely seismicity modulating trigger mechanism, the processes within and between clusters may also affect their behaviour. Clusters of small to moderate earthquakes can increase Coulomb stress on faults within or
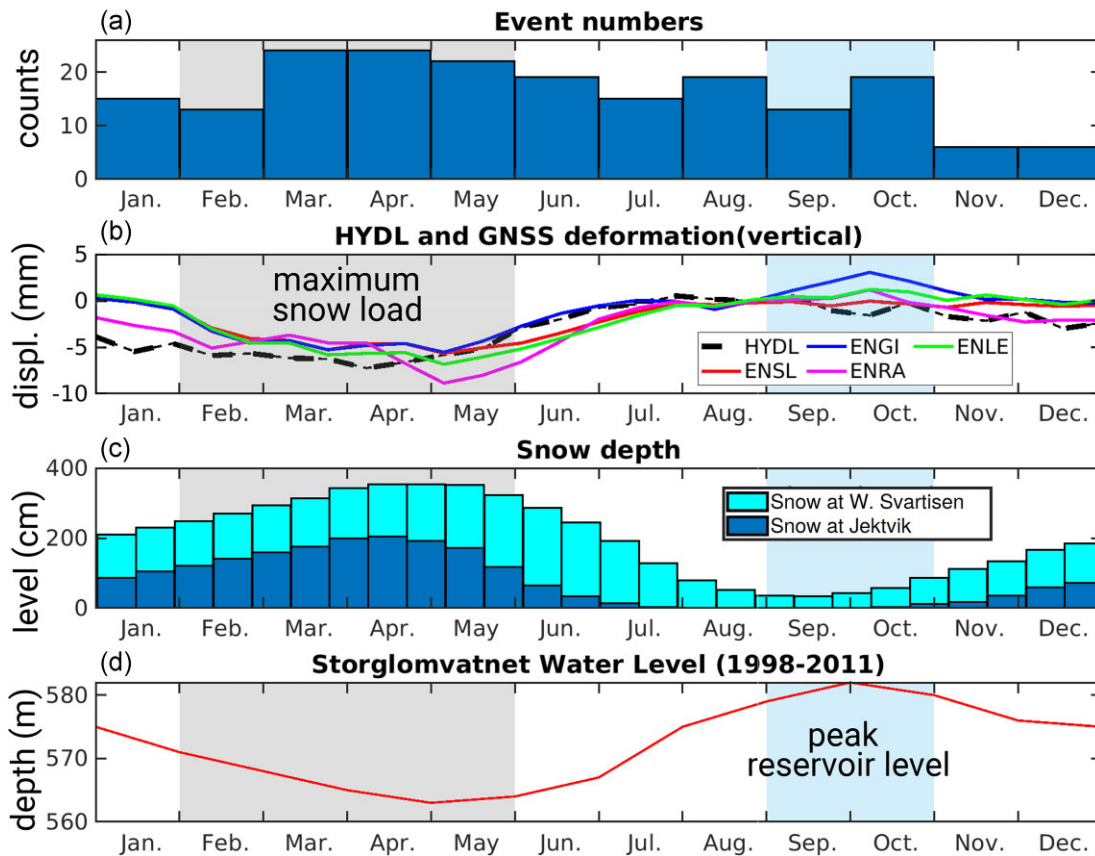
Figure 8. (a) Stack of monthly event numbers for the center of Jektvk (Group A). (b) Weekly average of vertical displacement from HYDL for Jektvik (2010–2021) and continuous GNSS (Mid-2019 to early-2023) from four stations close to Jektvik region. Linear trend in the GNSS data is removed. (c) Weekly average of snow thickness at Jektvik and West Svartisen glacier obtained from Norwegian climatology and hydrology database (https://www.senorge.no/). The data are averaged over 10-d intervals. (d) Monthly average level of Storglomvatnet water reservoir for the period 1998–2011 obtained from Bønsnes *et al.* (2015). Time windows with maximum snow load and peak reservoir level are marked as gray and blue areas, respectively. Locations of GNSS stations are shown in Fig. 1(a).

on neighboring segments and bring them closer to failure (Gahalaut *et al.* 2004; Hauksson *et al.* 2017). In addition to ΔCFF, co-seismic pore-pressure increase caused by earthquakes in one segment can reduce the normal stress, hence can increase the ΔCFF.

In order to understand the ΔCFF effect due to earthquakes in one cluster on to the seismogenic faults of other clusters, we performed simple but representative modeling using the Coulomb 3.3 software (Lin & Stein 2004; Toda *et al.* 2005), ignoring the possibility of co-seismic pore-pressure change. We used a cumulative fault source in a cluster following the approach of Gahalaut *et al.* (2004, 2022). We modeled ΔCFF due to slip on the NNE–SSW oriented normal fault, simulating a typical earthquake cluster source of the Jektvik swarm. We used the maximum cumulative M_0 of 1.03E+14 Nm, which is equivalent to M_w 3.3. Based on the scaling relation for SCR dip-slip earthquakes of Leonard (2010), we used a length of 400 m and downdip width of the source fault as 400 m and assumed a normal slip of 2 cm. We resolved ΔCFF on faults with orientation similar to the source fault. As expected, the modeling result shows increasing ΔCFF at the tip of the source faults (King *et al.* 1994). This implies that ΔCFF will increase on normal fault segments which are sub-parallel and are almost aligned with the source fault (Fig. 10). This simple model can explain the fault interaction through stress transfer and triggering of seismic events in between clusters. For example, cumulative ΔCFF generated by events in cluster A1 can trigger seismicity in clusters A4, B1, B3 and possibly later events in group

D. Additionally, triggering of parallel segments will be effective if the receiver faults are shallower or deeper than the source faults. This condition can explain the triggering of clusters A2 and A3 due to cumulative ΔCFF from cluster A1.

In light of the ΔCFF modeling, we hypothesize that seasonal load changes are able to trigger and modulate the seismicity. Once a cluster becomes active, it can possibly trigger earthquakes in neighboring clusters. These processes help to promote seismic rupture where the fracture system is already in a critically stressed state in response to present day stresses. Therefore, small increase in ΔCFF can trigger the swarm activity. Pore-pressure changes due to load changes and co-seismic processes are likely to play a role and can further promote failure (Gahalaut *et al.* 2022). However, given that hydrological loading appears to be the dominant times-dependent process and considering location uncertainties, it is not possible to test the contribution of additional processes on this complex swarm sequence using widely used modelling schemes (e.g. Shapiro *et al.* 1997; Shapiro 2015).

6 CONCLUSIONS

We present detailed spatio-temporal and seismogenesis characterization of a seismic swarm sequence in Jektvik, northern Norway, using an enhanced earthquake catalogue that spans a period of 9
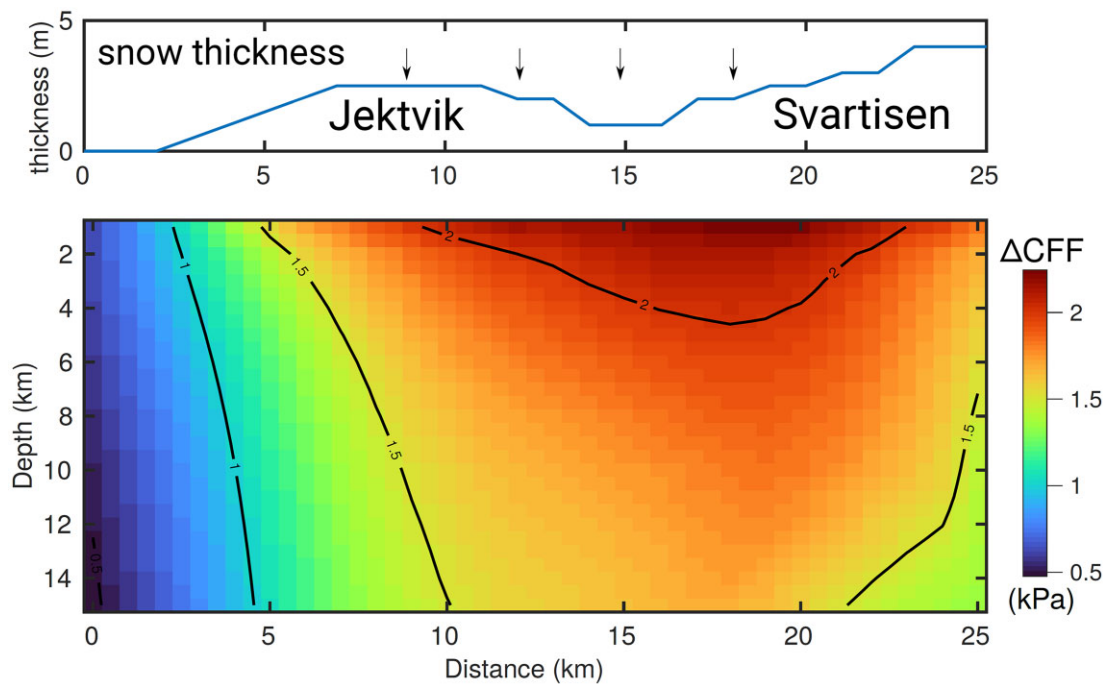
Figure 9. ΔCFF modeling result using a simple snow thickness model consists of two peaks in Jektvik and Svartisen. (a) 2D profile of the snow thickness used to calculate the ΔCFF due to snow load. (b) ΔCFF resolved on normal faults beneath Jektvik and Svartisen. Black lines are contours of ΔCFF with 0.5 kPa interval.

yr. The activity affected a relatively large area, but the overall moment release is relatively small. In this case, the active area was ca. 84 km^2, but the maximum earthquake magnitude was only M_L 3.2. The hypocenters were relocated and clustered using differential time data and waveform cross-correlation. The swarms occurred within an intricate system of NNE–SSW striking fluid-saturated fracture zones, where the earthquakes themselves are seen as failure of smaller fractures that are aligned with the orientation of the zones. This is apparent from the NNE–SSW trending normal fault mechanisms, which are a result of local extensional stresses and from the alignment of seismicity in the region. The seismicity trend matches the surface lineaments that are seen on high resolution terrain models. Based on precise locations and origin times, we combined earthquake clusters into four main groups. The relocated seismicity shows distinct spatio-temporal behaviours within and in between the groups. The seismic activity expanded progressively from the center, first toward SW and later toward east and NE. While the center of the sequence remained active during the entire observation period, the neighboring segments were mostly active only for a limited time.

Based on the coincidence of times of highest seismic activity and maximum hydrological load, we hypothesize that the hydrological load acts as a seasonal modulator. The seismic activity tends to increase between February and May, at the end of the northern hemisphere winter and beginning of spring. Vertical components of GNSS data show a maximum subsidence during this period, which correlates with the peak of snow load in the region. We show that the snow load increases the ΔCFF on the normal fault system and is possibly responsible for the seasonal modulation of seismicity. The response of each segment to this load is different, reflecting the ambient stress heterogeneity and fault characteristics. We further invoke the co-seismic ΔCFF as an additional process that promotes failure within and between fault segments.

DATA AVAILABILITY

Earthquake data catalogue from the Norwegian National Seismic Network (NNSN) is available at NNSN webpage (https://nnsn.geo.uib.no/nnsn/#/data/events/bulletins). Seismic data from NNSN (network code: NS; Ottemöller *et al.* 2021) and Neonor2 (2G; Michálek *et al.* 2018) are available at UiB-Norsar European Integrated Data Archive (EIDA) Node webpage (https://nnsn.geo.uib.no/nnsn/#/data/waveforms/access). Seismic data for Scanlips3D (ZR; England *et al.* 2016) network are archived at the Incorporated Research Institutions for Seismology (IRIS) Data Management Center (DMC; http://ds.iris.edu/ds/nodes/dmc/). Earthquake data were processed using EQtransformer package
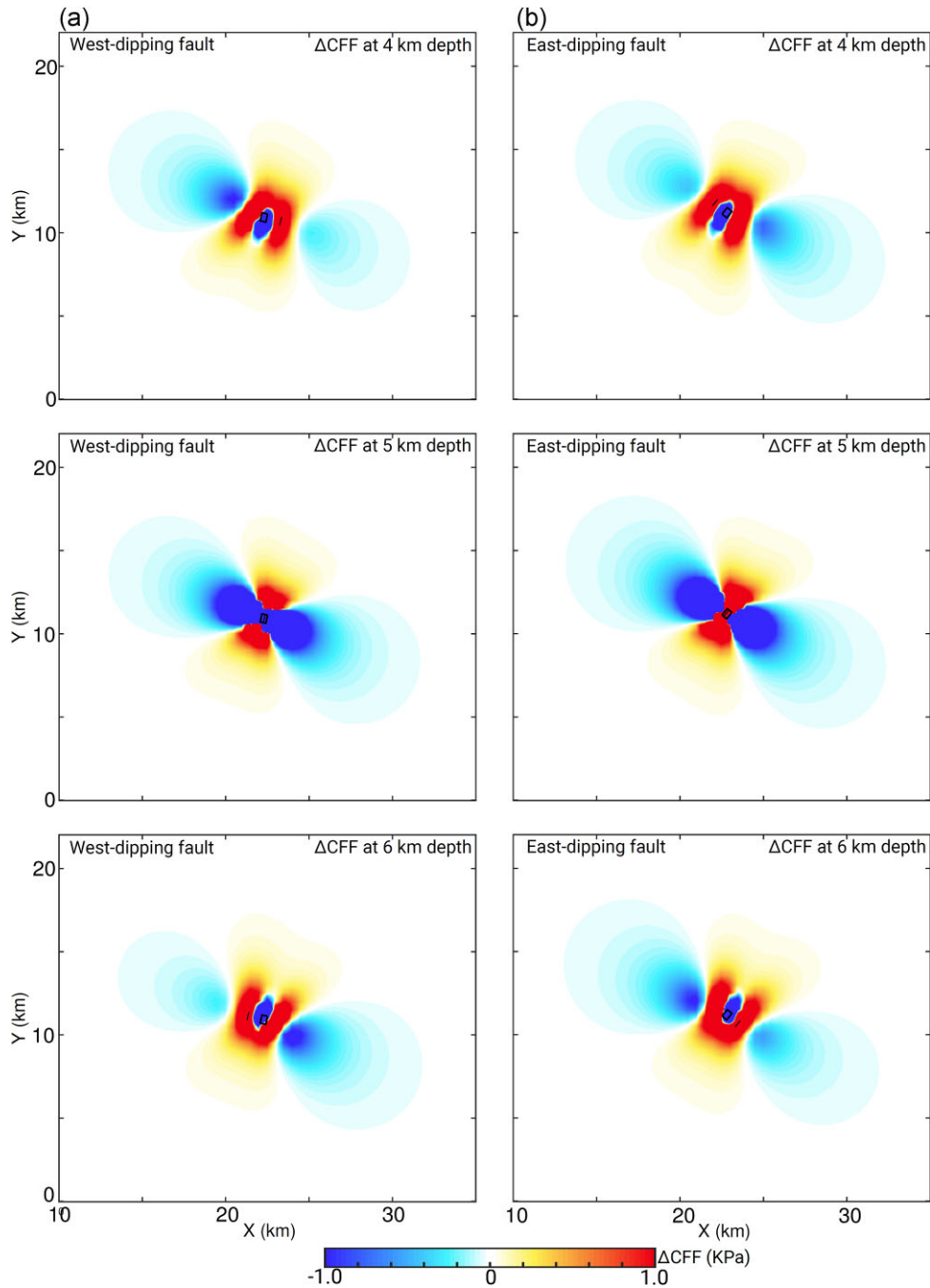
Figure 10. Coulomb stress change (ΔCFF) using a typical normal faulting earthquake in Jetkvik to show the possible inter-cluster triggering. The modeling was performed using using a normal event with M_w 3.3 with NNE–SSW strike. The ΔCFF are computed for west- and east-dipping planes with normal motion at 4, 5 and 6 km depth. The causative faults are depicted as black rectangles.

(https://eqtransformer.readthedocs.io), eqcorrscan package (https://eqcorrscan.readthedocs.io), Obspy package (https://docs.obspy.org/; https://doi.org/10.5281/zenodo.1040770) and Seisan earthquake analysis software (http://seisan.info/). The Norwegian bedrock geology map (Geological Survey of Norway 2011) is available at Geological Survey of Norway portal (https://geo.ngu.no/kart/berggrunn_mobil). Digital Terrain Model images are available at Norwegian mapping authority (Kartverket) portal (https://hoydedata.no/LaserInnsyn/ and https://www.geonorge.no/). The HYDL model is available at ftp://esmdata.gfz-potsdam.de/LOADING. Snow depth data is available at SeNorge portal (https://www.senorge.no/). The processed GNSS data are available from Nevada Geodetic Laboratory webpage (http://geodesy.unr.edu/magnet.php). Figures in this article were created using Matlab (https://www.mathworks.com/products/matlab.html), Generic Mapping Tools (Wessel *et al.* 2013), QGIS software (QGIS Development Team 2021) and Inkscape, a vector graphics editor (https://inkscape.org/). Earthquake catalogue used in this study is available at Zenodo https://doi.org/10.5281/zenodo.7101184.

SUPPORTING INFORMATION

Supplementary data are available at *GJI* online.

suppl_data

Please note: Oxford University Press is not responsible for the content or functionality of any supporting materials supplied by the authors. Any queries (other than missing material) should be directed to the corresponding author for the paper.

REFERENCES

Alsaker, A., Kvamme, L.B., Hansen, R.A., Dahle, A.& & Bungum, H., 1991. The ML scale in Norway, *Bull. seism. Soc. Am.,* **81**(2), 379–398.

Andajani, R.D., Tsuji, T., Snieder, R.& & Ikeda, T., 2020. Spatial and temporal influence of rainfall on crustal pore pressure based on seismic velocity monitoring, *Earth, Planets and Space,* **72**(1), 177 . doi:10.1186/s40623-020-01311-1.

Atakan, K., Lindholm, C.D.& & Havskov, J., 1994. Earthquake swarm in Steigen, northern Norway: an unusual example of intraplate seismicity, *Terra Nova,* **6**(2), 180–194.

Beyreuther, M., Barsch, R., Krischer, L., Megies, T., Behr, Y.& & Wassermann, J., 2010. ObsPy: A Python Toolbox for Seismology, *Seismol. Res. Lett.,* **81**(3), 530–533.

Bisrat, S., DeShon, H.R.& & Rowe, C., 2012. Microseismic Swarm Activity in the New Madrid Seismic Zone, *Bull. seism. Soc. Am.,* **102**(3), 1167–1178.

Bønsnes, T.E., Elvehøy, H., Vatne, A.& & Kvambekk, Å., 2015. *Oppdragsrapport A: Storglomfjordutbyggingen Hydrologiske undersøkelser i 2014,* Norges vassdrags- og energidirektorat, Oslo

Bungum, H.& & Olesen, O., 2005. The 31st of August 1819 Lurøy earthquake revisited, *Norwegian J. Geol.,* **85**(3): 245–252.

Bungum, H., Hokland, B.K., Husebye, E.S.& & Ringdal, F., 1979. An exceptional intraplate earthquake sequence in Meløy, Northern Norway, *Nature,* **280,** 32–35. https://www.nature.com/articles/280032a0#citeas

Bungum, H., Vaage, S.& & Husebye, E.S., 1982. The Meløy earthquake sequence, northern Norway: source parameters and their scaling relations, *Bull. seism. Soc. Am.,* **72**(1), 197–206.

Bungum, H., Olesen, O., Pascal, C., Gibbons, S., Lindholm, C.& & Vestøl, O., 2010. To what extent is the present seismicity of Norway driven by post-glacial rebound?, *J. Geol. Soc.,* **167**(2), 373–384.

Büyükakpınar, P., Cesca, S., Hainzl, S., Jamalreyhani, M., Heimann, S.& & Dahm, T., 2021. Reservoir-Triggered Earthquakes Around the Atatürk Dam (Southeastern Turkey), *Frontiers in Earth Science,* **9,** doi:10.3389/feart.2021.663385.

Castro, A., 2013. Tonalite–granodiorite suites as cotectic systems: A review of experimental studies with applications to granitoid petrogenesis, *Earth-Sci. Rev.,* **124,** 68–95.

Chamberlain, C.J., Hopp, C.J., Boese, C.M., Warren-Smith, E., Chambers, D., Chu, S.X., Michailos, K.& & Townend, J., 2017. EQcorrscan: Repeating and Near-Repeating Earthquake Detection and Analysis in Python, *Seismol. Res. Lett.,* **89**(1), 173–181.

Christiansen, L.B., Hurwitz, S.& & Ingebritsen, S.E., 2007. Annual modulation of seismicity along the san andreas fault near parkfield, ca, *Geophys. Res. Lett.,* **34**(4) doi:10.1029/2006GL028634.

Corfu, F., Andersen, T.B.& & Gasser, D., 2014. The Scandinavian Caledonides: main features, conceptual advances and critical questions, *Geol. Soc. London Special Publ.,* **390**(1), 9–43.

Costain, J.K., 2017. Groundwater recharge as the trigger of naturally occurring intraplate earthquakes, *Geol. Soc. London Special Publ.,* **432**(1), 91–118.

Craig, T.J., Chanard, K.& & Calais, E., 2017. Hydrologically-driven crustal stresses and seismicity in the New Madrid Seismic Zone, *Nature Commun.,* **8**(1), 2143. doi:10.1038/s41467-017-01696-w.

Demuth, A., Ottemöller, L.& & Keers, H., 2019. QLg wave tomography beneath Norway, *J. Seismol.,* **23,** 151–164

Deng, K., Zhou, S., Wang, R., Robinson, R., Zhao, C.& & Cheng, W., 2010. Evidence that the 2008 Mw 7.9 Wenchuan earthquake could not have been induced by the Zipingpu reservoir, *Bull. seism. Soc. Am.,* **100**(5B), 2805–2814.

Dill, R.& & Dobslaw, H., 2013. Numerical simulations of global-scale high-resolution hydrological crustal deformations, *J. Geophys. Res.: Solid Earth,* **118**(9), 5008–5017.

Drouin, V., Heki, K., Sigmundsson, F., Hreinsdóttir, S.& & Ófeigsson, B.G., 2016. Constraints on seasonal load variations and regional rigidity from continuous GPS measurements in Iceland, 1997–2014, *J. geophys. Int.,* **205**(3), 1843–1858

England, R.W., Ebbing, J. & Ben-Mansour, W., 2016. *SCANdinavian LIthosphere P and S wave experiment 3 D,* Tech. rep..NERC Geophysical Equipment. https://gef.nerc.ac.uk/documents/report/959.pdf

Fossen, H., 2010. Extensional tectonics in the North Atlantic caledonides: a regional view, in *Continental tectonics and mountain building: the legacy of Peach and Horne,* **335,** Geological Society of London, Bath

Gahalaut, K., Gahalaut, V., Bandari, N., Shekar, M., Sunilkumar, T.& & Srinagesh, D., 2022. Long duration non-volcanic and non-tectonic palghar earthquake swarm in the stable continental region of india—role of seasonal rainfall and earthquake cascading, *J. Seismol.* doi:10.1007/s10950-022-10087-8.

Gahalaut, V.K., Kalpna& & Singh, S.K., 2004. Fault interaction and earthquake triggering in the koyna-warna region, india, *Geophys. Res. Lett.,* **31**(11) doi:10.1029/2004GL019818.

Geological Survey of Norway, 2011. *Nasjonal berggrunnsdatabase.* Geological Survey of Norway, Trondheim

GEOMAP, 1990. *RV. 17 Tunnel Reppen - Strømdal: Resfraksjonsseismiske Målinger 1990 (In Norwegian),* Tech. rep. GEOMAP, Oslo.

Gibbons, S.J., Bøttger Sørensen, M., Harris, D.B.& & Ringdal, F., 2007. The detection and location of low magnitude earthquakes in northern Norway using multi-channel waveform correlation at regional distances, *Phys. Earth planet. Inter.,* **160**(3), 285–309.

Gradmann, S., Olesen, O., Keiding, M.& & Maystrenko, Y., 2018. *The Regional 3d Stress Field of Nordland, Northern Norway - Insights from Numerical Modelling, chap. Neotectonics in Nordland - Implications for petroleum exploration (NEONOR2),* Geological Survey of Norway, Trondheim.

Hainzl, S., Kraft, T., Wassermann, J., Igel, H.& & Schmedes, E., 2006. Evidence for rainfall-triggered earthquake activity, *Geophys. Res. Lett.,* **33**(19) doi:10.1029/2006GL027642.

Hauksson, E., Meier, M.-A., Ross, Z.E.& & Jones, L.M., 2017. Evolution of seismicity near the southernmost terminus of the San Andreas Fault: Implications of recent earthquake clusters for earthquake risk in southern California, *Geophys. Res. Lett.,* **44**(3), 1293–1301.

Havskov, J.& & Ottemoller, L., 1999. SeisAn Earthquake Analysis Software, *Seismol. Res. Lett.,* **70**(5), 532–534.

Havskov, J.& & Ottemöller, L., 2010. *Routine Data Processing in Earthquake Seismology: With Sample Data, Exercises and Software,* Springer, Dordrecht.

Havskov, J., Voss, P.H.& & Ottemöller, L., 2020. Seismological Observatory Software: 30 Yr of SEISAN, *Seismol. Res. Lett.,* **91**(3), 1846–1852.

Heki, K., 2003. Snow load and seasonal variation of earthquake occurrence in japan, *Earth Planet. Sci. Lett.,* **207**(1), 159–164.

Hicks, E.C., Bungum, H.& & Lindholm, C.D., 2000. Seismic activity, inferred crustal stresses and seismotectonics in the Rana region, Northern Norway, *Quaternary Science Reviews,* **19**(14), 1423–1436.

Hsu, Y.-J., Kao, H., Bürgmann, R., Lee, Y.-T., Huang, H.-H., Hsu, Y.-F., Wu, Y.-M.& & Zhuang, J., 2021. Synchronized and asynchronous modulation of seismicity by hydrological loading: A case study in Taiwan, *Sci. Adv.,* **7**(16), 1–12. doi:10.1126/sciadv.abf7282.

Janutyte, I., Lindholm, C.& & Olesen, O., 2017. Earthquake source mechanisms in onshore and offshore Nordland, northern Norway, *Norwegian J. Geol.,* **97**(3), 227–239.

Jiang, C., Zhang, P., White, M. C.A., Pickle, R.& & Miller, M.S., 2022. A Detailed Earthquake Catalogue for Banda Arc–Australian Plate Collision

Zone Using Machine-Learning Phase Picker and an Automated Workflow, *Seismic Rec.,* **2**(1), 1–10.

Kierulf, H.P., 2017. Analysis strategies for combining continuous and episodic GNSS for studies of neo-tectonics in Northern-Norway, *J. Geodyn.,* **109**, 32–40.

Kierulf, H.P., Steffen, H., Simpson, M. J.R., Lidberg, M., Wu, P.& & Wang, H., 2014. A GPS velocity field for Fennoscandia and a consistent comparison to glacial isostatic adjustment models, *J. Geophys. Res.: Solid Earth,* **119**(8), 6613–6629.

King, G. C.P., Stein, R.S.& & Lin, J., 1994. Static stress changes and the triggering of earthquakes, *Bull. seism. Soc. Am.,* **84**(3), 935–953.

Krischer, L., Megies, T., Barsch, R., Beyreuther, M., Lecocq, T., Caudron, C.& & Wassermann, J., 2015. ObsPy: A bridge for seismology into the scientific Python ecosystem, *Comput. Sci. Discovery,* **8**, 014003 doi:10.1088/1749-4699/8/1/014003.

Leonard, M., 2010. Earthquake Fault Scaling: Self-Consistent Relating of Rupture Length, Width, Average Displacement and Moment Release, *Bull. seism. Soc. Am.,* **100**(5A), 1971–1988.

Lienert, B.R.& & Havskov, J., 1995. A computer program for locating earthquakes both locally and globally, *Seismol. Res. Lett.,* **66**(5), 26–36.

Lin, J.& & Stein, R.S., 2004. Stress triggering in thrust and subduction earthquakes and stress interaction between the southern san andreas and nearby thrust and strike-slip faults, *J. Geophys. Res.: Solid Earth,* **109**(B2) doi:10.1029/2003JB002607.

Liu, M.& & Stein, S., 2016. Mid-continental earthquakes: Spatiotemporal occurrences, causes and hazards, *Earth-Sci. Reviews,* **162**, 364–386.

Lowry, A.R.& & Pérez-Gussinyé, M., 2011. The role of crustal quartz in controlling Cordilleran deformation, *Nature,* **471**(7338), 353–357.

Luckett, R., Ottemöller, L., Butcher, A.& & Baptie, B., 2018. Extending local magnitude ML to short distances, *J. geophys. Int.,* **216**(2), 1145–1156.

Mäntyniemi, P.B., Sørensen, M.B., Tatevossian, T.N., Tatevossian, R.E.& & Lund, B., 2020. A reappraisal of the Lurøy, Norway, earthquake of 31 August 1819, *Seismol. Res. Lett.* doi:10.1785/0220190363.

Matos, C., Custódio, S., Batló, J., Zahradník, J., Arroucau, P., Silveira, G.& & Heimann, S., 2018. An active seismic zone in intraplate west iberia inferred from high-resolution geophysical data, *J. Geophys. Res.: Solid Earth,* **123**(4), 2885–2907.

Maystrenko, Y., Brönner, M., Olesen, O., Saloranta, T.M.& & Slagstad, T., 2020. Atmospheric precipitation and anomalous upper mantle in relation to intraplate seismicity in Norway, *Tectonics,* **39**(9), e2020TC006070 doi:10.1029/2020TC006070.

Megies, T., Krischer, L., Chambers, D.J., Eulenfeld, T., Chamberlain, C.J., Lecocq, T.& & Barsch, R., 2019. ObsPy - A Python Library for Seismology, in *AGU Fall Meeting Abstracts,* Vol. **2019**, pp. American Geophysical Union. NS21A–12. https://ui.adsabs.harvard.edu/abs/2019AGUFMNS21A..12M/abstract

Mesimeri, M., Ganas, A.& & Pankow, K.L., 2022. Multisegment ruptures and Vp/Vs variations during the 2020–2021 seismic crisis in western Corinth Gulf, Greece, *J. geophys. Int.,* **230**(1), 334–348.

Michálek, J., Tjåland, N., Drottning, A., Strømme, M.L., Storheim, B.M., Rondenay, S.& & Ottemöller, L., 2018. *Report on seismic observations within the NEONOR2 project in the Nordland region, Norway (Aug. 2013 - May 2016), chap. Neotectonics in Nordland - Implications for petroleum exploration (NEONOR2),* Geological Survey of Norway, Trondheim.

Michelini, A.& & Bolt, B.A., 1986. Application of the principal parameters method to the 1983 Coalinga, California, aftershock sequence, *Bull. seism. Soc. Am.,* **76**(2), 409–420..

Münchmeyer, J. *et al.*, 2022. Which picker fits my data? a quantitative evaluation of deep learning based seismic pickers, *J. Geophys. Res.: Solid Earth,* **127**(1), e2021JB023499 . doi:10.1029/2021JB023499.

Mousavi, S.M., Sheng, Y., Zhu, W.& & Beroza, G.C., 2019. STanford EARthquake Data set (STEAD): A Global Data Set of Seismic Signals for AI, *IEEE Access,* **7**, 179464–179476. https://ieeexplore.ieee.org/document/8871127

Mousavi, S.M., Ellsworth, W., Weiqiang, Z., Chuang, L.& & Beroza, G., 2020. Earthquake transformer—an attentive deep-learning model for simultaneous earthquake detection and phase picking, *Nature Communications,* **11**, 3952 . doi:10.1038/s41467-020-17591-w.

Muir-Wood, R., 1989. The Scandinavian earthquakes of 22 December 1759 and 31 August 1819, *Disasters,* **12**(3): 223–236.

Ottemöller, L., Strømme, M.L.& & Storheim, B.M., 2018. *Seismic Monitoring and Data Processing at the Norwegian National Seismic Network, Vol. 52, chap. Summary of the Bulletin of the International Seismological Centre 2015 January-June,* pp. 27–40, International Seismological Centre, Thatcham, UK.

Ottemöller, L. *et al.*, 2021. UiB-NORSAR EIDA Node: Integration of Seismological Data in Norway, *Seismol. Res. Lett.,* **92**(3), 1491–1500.

Pollitz, F.F., Wech, A., Kao, H.& & Bürgmann, R., 2013. Annual modulation of non-volcanic tremor in northern cascadia, *J. Geophys. Res.: Solid Earth,* **118**(5), 2445–2459.

QGIS Development Team, 2021. *QGIS Geographic Information System,* QGIS Association. https://www.qgis.org

Roberts, D., 1988. The terrane concept and the Scandinavian Caledonides: a synthesis, *Norges Geologiske Undersøkelse Bulletin,* (413), 93–99.

Ross, Z.E., Cochran, E.S., Trugman, D.T.& & Smith, J.D., 2020. 3D fault architecture controls the dynamism of earthquake swarms, *Science,* **368**(6497), 1357–1361.

Rostad, H., 1990. *Strømdal Tunnel Sør: Ingeior Geologisk Rapport (In Norwegian),* Tech. rep, Statens Vegvesen Nordland, Bodø

Rutland, R. W.R.& & Sutherland, D.S., 1967. The chemical Composition of Granitic Gneisses and Spragmitic Meta-Sediments in the Glomfjord Region, Northern Norway., *Norsk Geologisk Tidsskrift,* **47**(4), 359–374.

Schoenball, M.& & Ellsworth, W.L., 2017. A systematic assessment of the spatiotemporal evolution of fault activation through induced seismicity in oklahoma and southern kansas, *J. Geophys. Res.: Solid Earth,* **122**(12), 10189–10206.

Shapiro, S.A., 2015. *Fluid-Induced Seismicity,* Cambridge Univ. Press, Cambridge.

Shapiro, S.A., Huenges, E.& & Borm, G., 1997. Estimating the crust permeability from fluid-injection-induced seismic emission at the KTB site, *J. geophys. Int.,* **131**(2), F15–F18.

Sharma, V. *et al.*, 2020. A long duration non-volcanic earthquake sequence in the stable continental region of India: The Palghar swarm, *Tectonophysics,* **779**, 228376. https://www.sciencedirect.com/science/article/pii/S0040195120300597

Shiddiqi, H.A., Tun, P.P.& & Ottemöller, L., 2019. Minimum 1D Velocity Model and Local Magnitude Scale for Myanmar, *Seismol. Res. Lett.,* **90**(5), 1923–1936.

Shiddiqi, H.A., Ottemöller, L., Rondenay, S., Halpaap, F., Gradmann, S.& & Michálek, J., 2022. Crustal structure and intraplate seismicity in Nordland, Northern Norway: Insight from Seismic Tomography, *J. geophys. Int.,* **230**, 813–830.

Shiddiqi, H.A., Ottemöller, L., Rondenay, S., Custódio, S., Halpaap, F.& & Gahalaut, V.K., 2023. Comparison of Earthquake Clusters in a Stable Continental Region: A Case Study from Nordland, Northern Norway, *Seismol. Res. Lett.* doi:10.1785/0220220325.

Snoke, J.A., 2003. FOCMEC: Focal mechanism determinations, Lee, W., Jennings, P., Kisslinger, C. & Kanamori, H.. *Int. Handbook Earthq. Eng. Seismol.,* **85**, Academic Press, London,1629–1630.

Snoke, J.A., 2017. *FOCMEC: FOCal MEChanism Determinations Manual.* Virginia Tech, Blacksburg.

Springer, A., Karegar, M.A., Kusche, J., Keune, J., Kurtz, W.& & Kollet, S., 2019. Evidence of daily hydrological loading in gps time series over europe, *J. Geod.,* **93**(10), 2145–2153.

Stein, S., Liu, M., Camelbeeck, T., Merino, M., Landgraf, A., Hintersberger, E.& & Kübler, S., 2017. Challenges in assessing seismic hazard in intraplate europe, *Geol. Soc. London Special Publ.,* **432**(1), 13–28.

Talwani, P., 2017. On the nature of intraplate earthquakes, *J. Seismol.,* **21**(1), 47–68.

Toda, S., Stein, R.S., Richards-Dinger, K.& & Bozkurt, S.B., 2005. Forecasting the evolution of seismicity in southern california: Animations built

on earthquake stress transfer, *J. Geophys. Res.: Solid Earth,* **110**(B5) doi:10.1029/2004JB003415.

Trugman, D.T.& & Shearer, P.M., 2017. Growclust: A hierarchical clustering algorithm for relative earthquake relocation, with application to the spanish springs and sheldon, nevada, earthquake sequences, *Seismol. Res. Lett.,* **88**(2A), 379–391.

Tsikalas, F., Faleide, J.I.& & Eldholm, O., 2001. Lateral variations in tectono-magmatic style along the Lofoten–Vesterålen volcanic margin off Norway, *Mar. Pet. Geol.,* **18**(7), 807–832.

Wang, Q.-Y., Brenguier, F., Campillo, M., Lecointre, A., Takeda, T.& & Aoki, Y., 2017. Seasonal crustal seismic velocity changes throughout japan, *J. Geophys. Res.: Solid Earth,* **122**(10), 7987–8002.

Wessel, P., Smith, W. H.F., Scharroo, R., Luis, J.& & Wobbe, F., 2013. Generic mapping tools: Improved version released, *EOS Trans. Am. Geophys. Union,* **94**(45), 409–410.